High-order accurate simulation of low-Mach laminar flow past two side-by-side cylinders with Spectral Difference method

Report ACL 2008-4

by

Chunlei Liang, Sachin Premasuthan & Antony Jameson

Aerospace Computing Laboratory

Aeronautics and Astronautics

Stanford University

May 2008

Abstract

This report presents development of a two-dimensional solver for compressible viscous flow using Spectral Difference (SD) method and its applications on simulating laminar flow past two cylinders. The high-order spectral difference solver is based on unstructured quadrilateral grids. High-order curved wall boundary representation is developed for cylinders. Two cylinders are aligned in side-by-side arrangements normal to freestream flow with different spacings (center-to-center distance/diameter s=2, 2.5, 3, 3.4 and 4). The simulation results are compared to experimental results (Williamson (1985); Zhou et al. (2001)) and other numerical results (Chang and Song (1990); Meneghini et al. (2001); Kang (2003); Ding et al. (2007)). As s increases, asymmetric, anti-symmetric and symmetric wake patterns are predicted. Force coefficients and Strouhal numbers are then correlated with wake patterns and compared to other published results.

Contents

List of Tables

List of Figures

Chapter 1

Introduction

1.1 Flow past two side-by-side cylinders

Investigations of the fluid flow and vertex dynamics about simple configurations of two cylinders help our understanding of the flows around more complex and larger-scale structures, for instance the flow around tube banks employed in process industries (Liang and Papadakis (2007)) and especially in the power generation and oil industry as well as flow around neighboring buildings and river flow vegetation, etc. Other applications such as hollow fiber arrays with many applications in absorption, extraction and ultra-filtration (Li et al. (2005)) or paper machine forming fabrics (Huang et al. (2006)). In the latter examples, the flows are laminar with Reynolds number in the order of 150-200.

Zdravkovich (1977, 1987) has reviewed the problem of mutual interference between pairs of cylinders in a steady flow. A lot attention is paid to the side-by-side and inline arrangements of the cylinder pair. Williamson (1985) suggested that the spacing between two side-by-side cylinders centers/diameter ($2 \leq s \leq 6$) are such as to produce vortex-shedding synchronization and the resulting wake configuration will be either two parallel streets in antiphase or a binary-vortex street which is a street being composed of pairs of like-signed vortices rotating around one another with Reynolds number in the order of 100-200. The experimental results obtained Zhou et al. (2001) at relatively low Reynolds numbers (150-450) also suggested that the flow pattern is very much independent of Reynolds number of this range. At s=3, they observed the anti-phase flow patterns for all Reynolds numbers using more advanced flow visualization methods. Chang and Song

(1990) made an early investigation of laminar flow past two side-by-side cylinders using a blending technique of Finite-Element method and Finite-Difference method. Recently, numerical simulations have been performed for incompressible laminar flow past two side-by-side cylinders by Meneghini et al. (2001) using finite-element unstructured method, Kang (2003) using finite-volume structured method with immersed boundary technique and Ding et al. (2007) using mesh-free finite-difference method.

The above studies mentioned are all about incompressible flows. The simulation codes commonly attained at best second-order accuracy in space. Furthermore, all the above discussed numerical simulations employed only piecewise linear wall boundary conditions or some kind of interpolation schemes to satisfy no-slip condition for immersed boundary method. The present simulation uses a recently developed Spectral Difference high-order unstructured method to simulate a low-Mach number compressible laminar flow past two side-by-side cylinders. A cubic spline curve fitting routine is programmed into our solver and it allows an automatic construction of a cubic curved wall boundary condition for each cylinder.

On the other hand, despite the small dependence on Reynolds number regarding the laminar wake flow pattern past the cylinder pair, near some critical spacing, the Reynolds number effect may prevail. As the above studies have reported either anti-symmetric or symmetric flow patterns for s=3 and Reynolds numbers 100, 150 and 200, this paper will make effort to clarify this aspect.

1.2 Spectral Difference method

Until recently, compressible flow computations on unstructured meshes have generally been dominated by schemes restricted to second order accuracy. However, the need for highly accurate methods in applications such as large eddy simulation, direct numerical simulation, computational aero-acoustics etc., has seen the development of higher order schemes for unstructured meshes such as the Discontinuous Galerkin (DG) Method (Cockburn and Shu (1989, 1998); Bassi and Rebay (1997)), Spectral Volume (SV) method (Wang (2002); Liu et al. (2006*b*); Wang and Liu (2006)) and Spectral Difference (SD) Method (Liu et al. (2006*a*); Wang et al. (2007); Liang et al. (2008)). The SD method

is a newly developed efficient high-order approach based on differential form of the governing equation. It was originally proposed by Liu et al. (2006a) and developed for wave equations in their paper on triangular grids. Wang et al. (2007) extended it to 2D Euler equations on triangular grids and Liang et al. (2008) improved the convergence of the method using implicit LU-SGS and p-multigrid schemes. Recently, Sun et al. (2007) further developed it for three-dimensional Navier-Stokes equations on hexahedral unstructured meshes. The SD method combines elements from finite-volume and finite-difference techniques. Similar to the discontinuous Galerkin (DG) and spectral volume (SV) methods, the SD scheme achieves high-order accuracy by locally approximating the solutions as a high degree polynomial inside each cell. However, being based on the differential form of the equations, its formulation is simpler than that of the DG and SV methods as no test function or surface integral is involved. Conservation properties are still maintained by a judicious placement of the nodes at quadrature points of the chosen simplex.

The paper is organized as follows. Chapter 2 describes the numerical approach and solution methods. In order to validate the spatial accuracy of the code, chapter 3 presents two cases with analytical solutions and simulation results obtained by SD method in addition to a simulation of flow past an isolated cylinder with detailed comparisons to other results. Chapter 4 reports the simulation results obtained for laminar viscous flows past two side-by-side cylinders. Finally, chapter 5 summarizes the main findings of this work.

Chapter 2

Numerical formulation

The formulation of the equations is similiar to the formulation of Sun et al. (2007) for unstructured hexahedral grids.

Consider the unsteady compressible 2D Navier Stokes equations in conservative form

$$\frac{\partial Q}{\partial t} + \frac{\partial F}{\partial x} + \frac{\partial G}{\partial y} = 0 \tag{2.1}$$

where Q is the vector of conserved variables; F and G are the total fluxes including both inviscid and viscous flux vectors. To achieve an efficient implementation, all elements in the physical domain (x, y) are transformed into a standard square element ($0 \leq \xi \leq 1$, $0 \leq \eta \leq 1$) as shown in figure 2.1. The transformation can be written as:

$$\begin{pmatrix} x \\ y \end{pmatrix} = \sum_{i=1}^{K} M_i(\xi, \eta) \begin{pmatrix} x_i \\ y_i \end{pmatrix} \tag{2.2}$$

where K is the number of points used to define the physical element, (x_i, y_i) are the cartesian coordinates of those points, and $M_i(\xi, \eta)$ are the shape functions. The metrics and the Jacobian of the transformation can be computed. The governing equations in the physical domain are then transferred into the computational domain, and the transformed equations take the following form:

$$\frac{\partial \tilde{Q}}{\partial t} + \frac{\partial \tilde{F}}{\partial \xi} + \frac{\partial \tilde{G}}{\partial \eta} = 0 \tag{2.3}$$

where $\bar{Q} = |J| \cdot Q$ and

$$\begin{pmatrix} \bar{F} \\ \bar{G} \end{pmatrix} = |J| \begin{pmatrix} \xi_x & \xi_y \\ \eta_x & \eta_y \end{pmatrix} \begin{pmatrix} F \\ G \end{pmatrix} \tag{2.4}$$

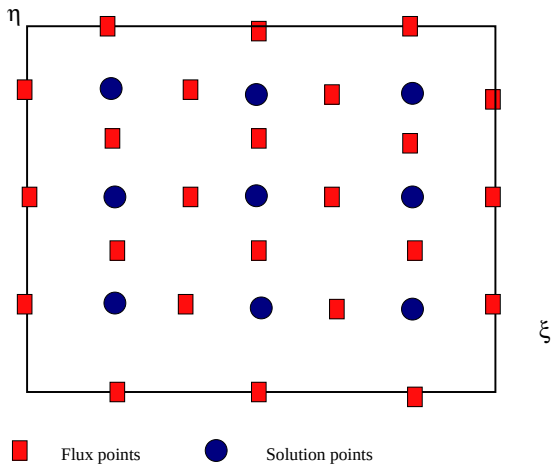

Figure 2.1: Distribution of flux and solution points for the third order SD scheme

In the standard element, two sets of points are defined, namely the solution points and the flux points, illustrated in figure 2.1.

In order to construct a degree $(N-1)$ polynomial in each coordinate direction, solution at N points are required. The solution points in 1D are chosen to be the Gauss points defined by:

$$X_s = \frac{1}{2}\left[1 - cos\left(\frac{2s-1}{2N}\cdot\pi\right)\right], s = 1, 2, \cdots, N. \tag{2.5}$$

The flux points are selected to be the Gauss-Lobatto points given by

$$X_{s+1/2} = \frac{1}{2}\left[1 - cos\left(\frac{s}{N}\cdot\pi\right)\right], s = 0, 1, \cdots, N. \tag{2.6}$$

Using the solutions at N solution points, a degree $(N-1)$ polynomial can be built using the following Lagrange basis defined as:

$$h_i(X) = \prod_{s=0, s\neq i}^{N}\left(\frac{X - X_s}{X_i - X_s}\right) \tag{2.7}$$

Similarly, using the fluxes at $(N+1)$ flux points, a degree N polynomial can be built for the flux using a similar Lagrange basis defined as:

$$l_{i+1/2}(X) = \prod_{s=0, s\neq i}^{N}\left(\frac{X - X_{s+1/2}}{X_{i+1/2} - X_{s+1/2}}\right) \tag{2.8}$$

The reconstructed solution for the conserved variables in the standard element is just the tensor products of the two one-dimensional polynomials,

$$Q(\xi, \eta) = \sum_{j=1}^{N}\sum_{i=1}^{N}\frac{\tilde{Q}_{i,j}}{|J_{i,j}|}h_i(\xi)\cdot h_j(\eta) \tag{2.9}$$

Similarly, the reconstructed flux polynomials take the following form:

$$\begin{aligned}\tilde{F}(\xi,\eta) &= \sum_{j=1}^{N}\sum_{i=0}^{N}\tilde{F}_{i+1/2,j}l_{i+1/2}(\xi)\cdot h_j(\eta),\\ \tilde{G}(\xi,\eta) &= \sum_{j=0}^{N}\sum_{i=1}^{N}\tilde{G}_{i,j+1/2}h_i(\xi)\cdot l_{j+1/2}(\eta)\end{aligned} \tag{2.10}$$

The reconstructed fluxes are only element-wise continuous, but discontinuous across cell interfaces. For the inviscid flux, a Riemann solver is employed to compute a common flux at interfaces to ensure conservation and stability. In our case, we have used the Rusanov solver Rusanov (1961) to compute the interface fluxes.

In summary, the algorithm to compute the inviscid flux derivatives consists of the following steps:

1. Given the conservative variables at the solution points, the conservative variables are computed at the flux points

2. The inviscid fluxes at the interior flux points are computed using the solutions computed at Step (1)

3. The inviscid fluxes at the element interfaces are computed using the Rusanov solver. Given the normal direction of the interface n, and the averaged normal velocity component V_n and the sound speed c, the inviscid flux on the interface can be determined.

4. The derivatives of the fluxes are computed at the solution points using the derivatives of Lagrange operators l

$$\begin{aligned}\left(\frac{\partial\tilde{F}}{\partial\xi}\right)_{i,j} &= \sum_{r=0}^{N}\tilde{F}_{r+1/2,j}\cdot l'_{r+1/2}(\xi_i),\\ \left(\frac{\partial\tilde{G}}{\partial\eta}\right)_{i,j} &= \sum_{r=0}^{N}\tilde{G}_{i,r+1/2}\cdot l'_{r+1/2}(\eta_j)\end{aligned} \tag{2.11}$$

We consider two-dimensional Navier-Stokes equations written in conservation form as the one described in Sun et al. (2006)

$$\frac{\partial Q}{\partial t}+\nabla F_e(Q)-\nabla F_v(Q,\nabla Q)=0 \tag{2.12}$$

where the conservative variables Q and Cartesian components $f_e(Q)$ and $g_e(Q)$ of the inviscid flux vector $F_e(Q)$ are given by

$$Q = \begin{Bmatrix} \rho \\ \rho u \\ \rho v \\ E \end{Bmatrix}, \quad f_e(Q) = \begin{Bmatrix} \rho u \\ \rho u^2 + p \\ \rho uv \\ u(E+p) \end{Bmatrix}, \quad g_e(Q) = \begin{Bmatrix} \rho v \\ \rho uv \\ \rho v^2 + p \\ v(E+p) \end{Bmatrix} \tag{2.13}$$

Here ρ is the density, u and v are the velocity components in x and y directions, p stands for pressure and E is the total energy. The pressure is related to the total energy by

$$E = \frac{p}{\gamma - 1} + \frac{1}{2}\rho(u^2 + v^2) \tag{2.14}$$

with a constant ratio of specific heat γ. For all test cases in the present study, γ is going to be 1.4 for air.

The Cartesian components $f_v(Q, \nabla Q)$ and $g_v(Q, \nabla Q)$ of viscous flux vector $F_v(Q, \nabla Q)$ are given by

$$f_v(Q, \nabla Q) = \mu \begin{Bmatrix} 0 \\ 2u_x + \lambda(u_x + v_y) \\ v_x + u_y \\ u[2u_x + \lambda(u_x + v_y)] + v(v_x + u_y) + \frac{C_p}{P_r} T_x \end{Bmatrix},$$

$$g_v(Q, \nabla Q) = \mu \begin{Bmatrix} 0 \\ v_x + u_y \\ 2v_y + \lambda(u_x + v_y) \\ v[2v_y + \lambda(u_x + v_y)] + u(v_x + u_y) + \frac{C_p}{P_r} T_y \end{Bmatrix} \tag{2.15}$$

where μ is the dynamic viscosity, C_p is the specific heat and P_r stands for Prandtl number. T is temperature which can be derived from the perfect gas assumption. λ is set to $-2/3$ according to the Stokes hypothesis.

The solution procedures to get viscous fluxes can be described as the following steps.

- reconstruct $Q_{k,i}$ at the flux points from the conservative variables at the solution points using equation 2.9.

- average the field of $Q_{k,i}$ on the element interfaces as $\overline{Q_f} = \frac{1}{2}(Q^L_{k,i}+Q^R_{k,i})$. Meanwhile, boundary conditions shall be applied for u, v and T.

- ∇u, ∇v and ∇T can be evaluated from $\overline{Q_f}$ using equation 2.11 where $\nabla Q = \left\{ \begin{array}{c} Q_x \\ Q_y \end{array} \right\}$ and $Q_x = \frac{\partial Q}{\partial \xi}\xi_x + \frac{\partial Q}{\partial \eta}\eta_x$, etc.

- reconstruct ∇u, ∇v and ∇T from equation 2.9 and average them on the element interfaces as $\overline{\nabla Q_f} = \frac{1}{2}(\nabla Q^L_{k,i} + \nabla Q^R_{k,i})$

- with $\overline{Q_f}$ and $\overline{\nabla Q_f}$, we are ready to compute viscous flux vectors described in equation 2.15 at the element interfaces.

Flows with either steady or unsteady solutions are considered in this paper. In order to solve the flow to a steady state from a nearly arbitrary initial guess, a relaxation scheme is needed. Therefore, the time derivative term is kept for all cases. All computations in this paper are advanced in time using a fourth-order strong-stability-preserving five-stage Runge-Kutta scheme (Spiteri and Ruuth (2002)).

Chapter 3

Accuracy validation

In the following, an inviscid flow case and a viscous flow case with analytical solutions are selected in order to demonstrate the order of accuracy of the implemented SD method for both flux vectors in equation 2.12. It is followed by a classical testing case about laminar flow past an isolated cylinder at Re=100.

3.1 Validation using supersonic vortex flow

The supersonic vortex flow problem is one of the few non-trivial problems of the compressible 2D Euler equations for which a smooth analytical solution is known. The inviscid, isentropic, supersonic flow of a compressible fluid between concentric circular arcs presents a flow where the velocity varies inversely with radius. The expression for density as a function of radius r is given by:

$$\rho\left(r\right)=\rho_i\left\{1+\frac{\gamma-1}{2}M_i^2\left[1-\left(\frac{r_i}{r}\right)^2\right]\right\}^{\frac{1}{\gamma-1}} \tag{3.1}$$

where M_i and r_i are the Mach number and the radius at the inner arc. In the present calculation, the Mach number, density and pressure at the inner radius r_i are specified to be 2.25, 1 and $1/\gamma$ respectively. The inner and outer radii are 1 and 1.384. The outer arc and bottom boundaries are fixed with analytical solutions. The zero-gradient extrapolation boundary is employed for the exit. In the following, the numerical solution to this problem are computed for 2nd, 3rd and 4th order SD method on successively refined grids. All the computations are initialized using constant density and pressure. The $L2$ error of the density is evaluated.

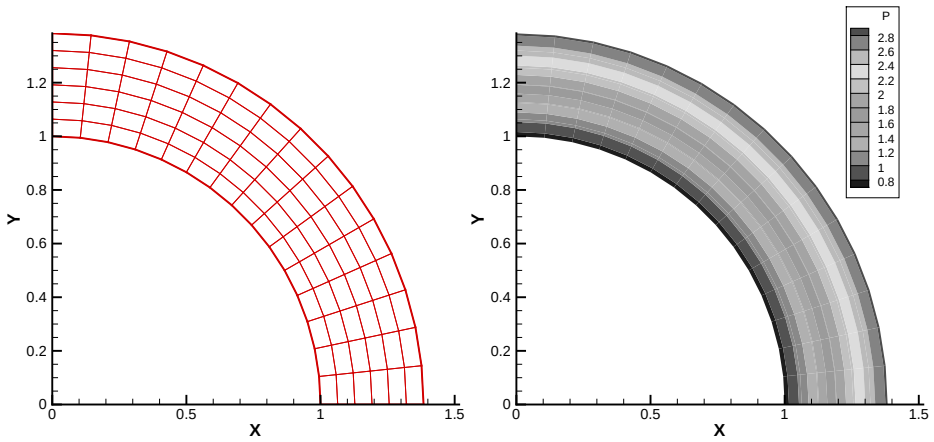

(a) (b)

Figure 3.1: Supersonic vortex flow obtained using grid of 6×15

The four meshes used in the computation were of sizes 10×4, 15×6, 30×12, and 60×24. A sample 15×6 mesh is shown in figure 3.1 (a). Figure 3.1 (b) shows the pressure contours in the flow field obtained by 3rd order SD method. The details of the order calculation and verification are shown in Table 3.1. The tables clearly indicate that the SD method applied to the steady compressible Euler equations exhibits a full order of convergence on smooth solutions. It provides the details of the spatial accuracy of the SD method for different orders for this numerical experiment. One can also see the $L2$-error of the SD method at different order SD method against the number of degrees of freedom. One can also clearly see that a higher order SD method requires a less number of degrees of freedom than a lower order SD method to achieve the same accuracy.

3.2 Validation using compressible Couette flow

The numerical order of accuracy is validated using compressible Couette flow with analytical solution. A grid with 4×2 cells is shown in figure 3.2. A periodic boundary condition is used in the stream-wise direction. A moving wall no-slip boundary with constant temperature and a specified external pressure is used for the top surface. A stationary no-slip wall with constant temperature is used for the bottom surface. We obtained desired numerical order $L2$ accuracy as shown in table 3.2.

Having validated the order of spatial accuracy using testing problems with steady flow

No. of elements	No. of DOFs	L2-error	Order
2nd order SD			
40	160	4.7249E-03	-
90	360	1.9881E-03	2.135
360	1440	4.4721E-04	2.152
1440	5760	1.0196E-04	2.133
3rd order SD			
40	360	3.3393E-04	-
90	810	9.8833E-05	3.003
360	3240	1.2242E-05	3.013
1440	12960	1.5230E-06	3.007
4th order SD			
40	640	1.9238E-05	-
90	1440	3.7883E-06	4.008
360	5760	2.3651E-07	4.002
1440	23040	1.4743E-08	4.004

Table 3.1: L^2 errors and orders of accuracy of inviscid supersonic vertex flow

solutions, we simulate the unsteady flow past an isolated cylinder at Re=100 and compare to other results in detail.

3.3 Viscous flow past one cylinder

Figure 3.4 shows the computational grid for the unsteady flow past a single cylinder. There are 32 cells around the circumference of the cylinder. The first cell near to the cylinder wall has a spacing around 11% cylinder radius in the normal direction. The level of grid resolution is very close to the one used in Meneghini et al. (2001) who employed 128 points around the cylinder wall and the first node had a distance about 1% of cylinder radius for an isolated cylinder case. The computation for this case is performed using fifth-order SD method and a cubic curved wall boundary condition is employed for the cylinder surface. Dirichlet boundary condition is used for the inlet and fixed-pressure is

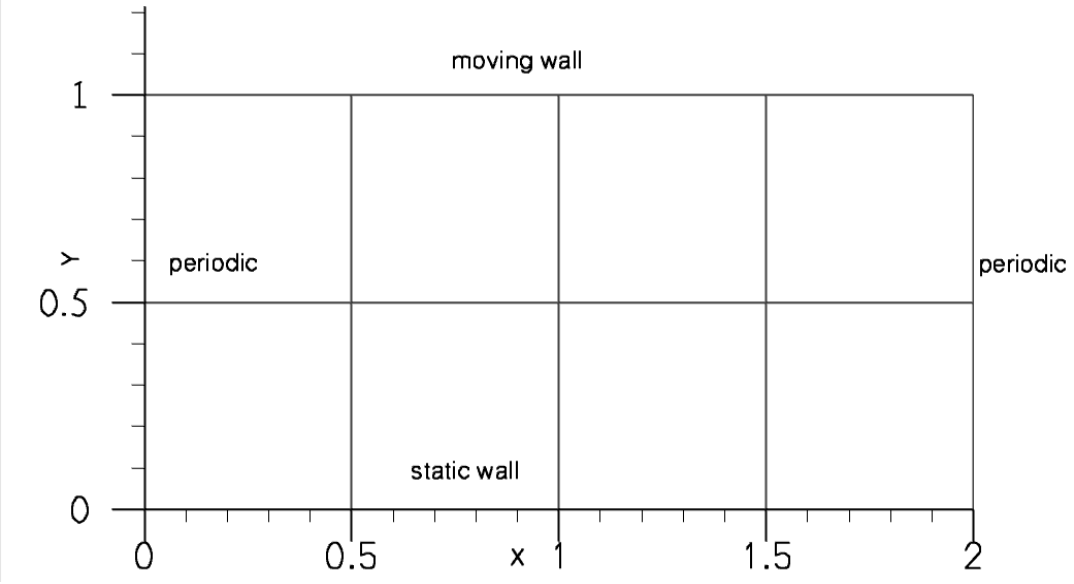

Figure 3.2: Grid 4×2 for Couette Flow and boundary conditions

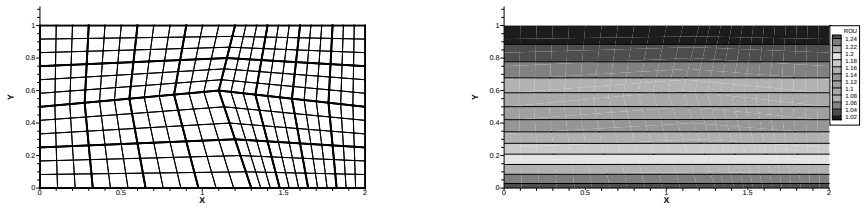

(a) Grid 8×4 (b) density contour

Figure 3.3: Compressible Couette flow grid and its solution for density field.

No. of elements	No. of DOFs	L2-error	Order
2nd order SD			
2	8	1.4180E-02	-
8	32	3.3520E-03	2.081
32	128	9.1210E-04	1.878
128	512	2.4350E-04	1.905
3rd order SD			
2	18	1.4783E-03	-
8	72	1.5199E-04	3.282
32	288	1.6525E-05	3.201
128	1152	1.7991E-06	3.199
4th order SD			
2	32	1.9784E-04	-
8	128	1.1827E-05	4.064
32	512	7.9780E-07	3.890
128	2048	4.7330E-08	4.075

Table 3.2: L^2 errors and orders of accuracy of viscous Couette flow

adopted for the outlet boundary condition. Invisicd symmetry boundary conditions are applied on the two lateral sides.

One snapshot of pressure contour and velocity streamlines are illustrated in figure 3.5. The vortex formed by the fluid from the bottom of the cylinder is associated with a region of low pressure. At this time instant, the unsteady lift coefficient attains its minimum. SD method offers great flexibility in grid-independence study. The only parameter to tune in our solver is the polynomial degree N. The differences of coefficients $C_l^{'}$ and $C_d^{'}$ predicted by 4th-order (total DOFs 21,376) and fifth-order SD methods (total DOFs 33,400) are both less than 2%. In the following for an isolated cylinder case, we only present the results obtained by fifth-order SD method.

Table 3.3 reports the comparison between present computation of compressible viscous flow at Mach number 0.2 to other numerical and experimental studies for incompressible

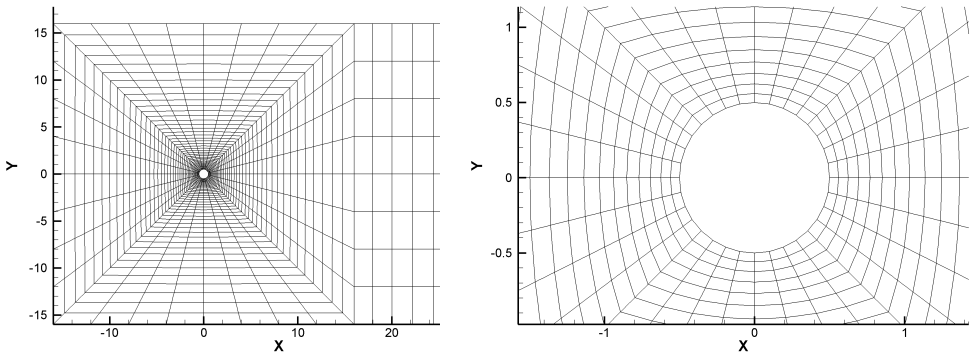

(a) (b)

Figure 3.4: Computational grid for unsteady flow past a cylinder

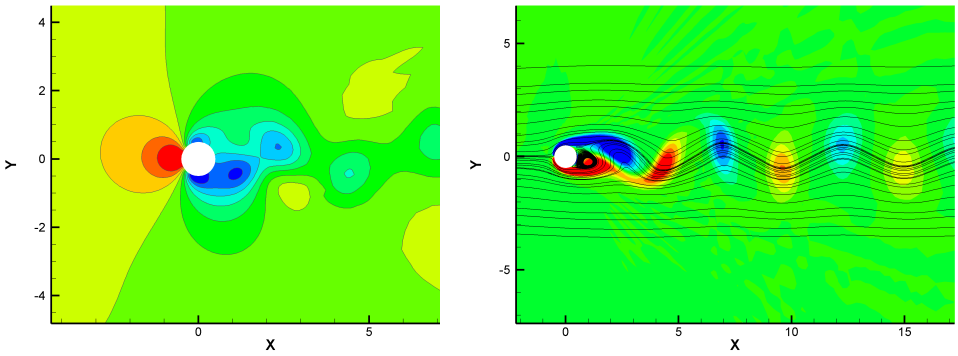

(a) pressure contour (b) streamlines

Figure 3.5: Instantaneous flow field computed for flow past a cylinder

Investigator	Present	Sharman 05	Mene- 01	Kang (2003)	Ding 07
Re no.	100	100	100	100	100
nodes	1,336	14,441	13,696	62,127	23,033
blockage	0.0312	0.02	0.047	-	-
C_l'	0.232	0.23	-	0.32	0.287
$\overline{C_d}$	1.365	1.33	1.37	1.33	1.356
C_d'	0.0086	0.0064	-	-	0.01
St. no.	0.164	0.164	0.165	0.165	0.166

Table 3.3: Comparison of present results against other results for flow over a cylinder at Reynolds number 100

viscous flow at the same Reynolds number 100. The Strouhal number predicted by present SD method on a mesh with degree-of-freedom 33,400 is identical to the one predicted by Sharman et al. (2005) and the measured value by Williamson (1989). There is a separate compressible flow simulation which is not included in the table. Mittal and Tezduyar (1998) also predicted 0.164 using a finite-element compressible flow solver at Re=100 and Mach number 0.2. The fluctuating lift coefficient is identical to the one predicted by the incompressible solver of Sharman et al. (2005). Kang (2003); Ding et al. (2007) predicted higher C_l' probably due to insufficient near wall grid resolution and lower-order spatial piecewise schemes which are unable to resolve the wall curvature. The mean and rms drag coefficients are slightly higher than the ones predicted by Sharman et al. (2005). However, the presently predicted $\overline{C_d}$ 1.365 is close to 1.37 predicted by Meneghini et al. (2001) and 1.356 predicted by Ding et al. (2007). The low compressibility of the present flow condition may also slightly affect mean drag coefficient but its impact is certainly not noticeably strong. Mittal and Tezduyar (1998) also predicted the mean C_d around the level of 1.4 as can be seen from figure 7 in their paper for Mach 0.2 and Re=100. Overall, this validation proves that our 2D spectral difference method produces the correct physics for flow past a cylinder.

Chapter 4

Flow past two side-by-side cylinders

4.1 Computational condition

In the following, we report simulations of flow past two side-by-side cylinders using either third-order or 4th-order accurate SD methods. Iso-thermal wall boundary condition is employed for temperature field. Dirichlet boundary condition is applied for the left inlet boundary. The top and bottom boundaries use symmetrical slip condition. For the right boundary, fixed pressure is specified and other values are extrapolated. If not emphasized elsewhere, the time step size for all computations $\frac{\Delta t U_\infty}{D} = 8 \times 10^{-4}$.

Simulations have been carried out with two cylinders in a side-by-side arrangement for gaps/diameter in the range $2 \leq s \leq 4$. The point with coordinate (0,0) is located at the middle distance between the cylinders. The free-stream Mach number is 0.2 and Reynolds number is 100 or 200. As shown in figure 4.1, the typical computational grid for s=3 case has cell number 5,106 (total DOFs are 45,954 and 81,696 for 3rd-order and 4th-order SD methods respectively). There is only 60 cells around the periphery of a cylinder surface but this number is already nearly double of the one used for the isolated cylinder testing case. The first cell near the cylinder wall is located at a distance of about 2.8% of the cylinder radius. However, considering third-order SD method and a cubic curved boundary condition applied for the wall, the present simulation has a finer resolution than Meneghini et al. (2001) who employed 128 points around the cylinder wall and the first node had a distance about 1% of cylinder radius. The present near wall grid resolution is even finer than the one used by Kang (2003) with immersed boundary method.

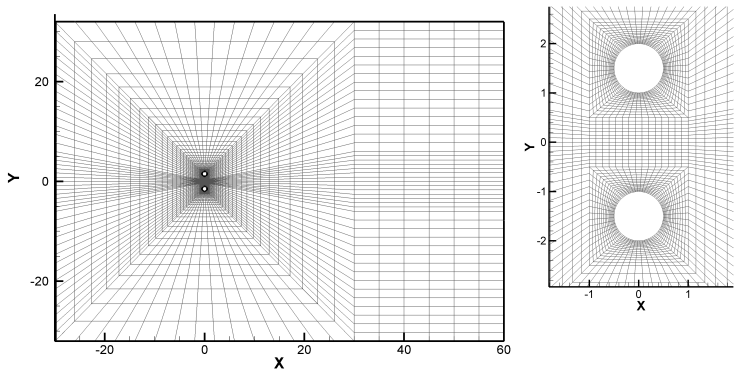

(a) complete domain (b) details around the cylinder

Figure 4.1: Computational grid for unsteady flow past two side-by-side cylinders

4.2 Wake dynamics

When $s \leq 2$, it is known that the near wake of the cylinder pair is asymmetric and the gap flow becomes biased. Figure 4.2 (a) and (b) shows the upward and downward biased gap flows respectively. The individual vortex street does not exist any longer but the merged vortices establish a single wake as if they had originated from a single body. When the gap flow is deflected downwards, the lower cylinder has a bigger C_d and higher shedding frequency than the upper one since the lower cylinder is relatively in suction pressure (see figure 4.3). This is in a good agreement with the experimental observation of Bearmann and Wadcock (1973). The lift coefficient shown in figure 4.3 also indicates that the higher-drag cylinder is having a higher shedding frequency. Two Strouhal numbers 0.175 and 0.225 are identified through Fourier transformation. The former one is close to the one predicted by Kang (2003).

Figures 4.4 and 4.5 demonstrate the transition of vortex shedding wake pattern from symmetric anti-phase regime to anti-symmetric in-phase regime at Reynolds number 100. The cylinder spacings are s=2.5 and s=3 respectively. Initially, the lift coefficients for both cylinders are in antiphase (of 180°phase difference) and gradually the difference reduces and converges to in-phase (0°phase difference). Chang and Song (1990) also observed from the time history of C_l that the vortex drifts with time from the anti-phase regime to in-phase regime.

Figure 4.6 defines four-phase snapshots for an in-phase vortex shedding period for s=2.5 and Re=100 case using the time history of C_l. Figure 4.7 visualizes the streamlines

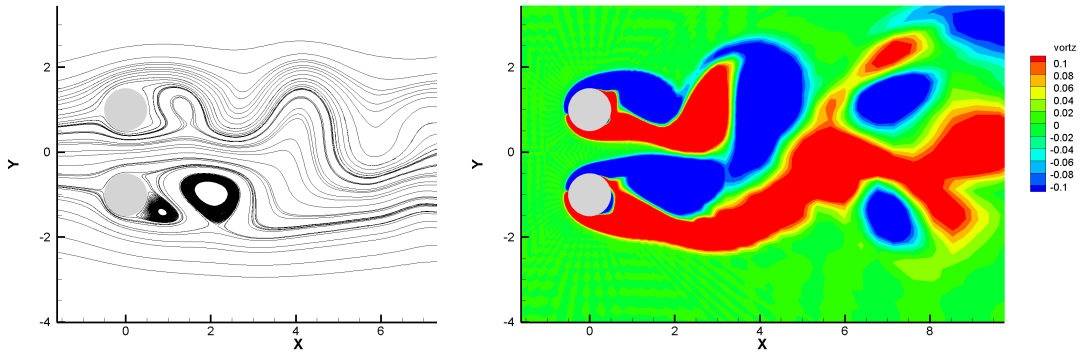

(a) streamlines (a) vorticity

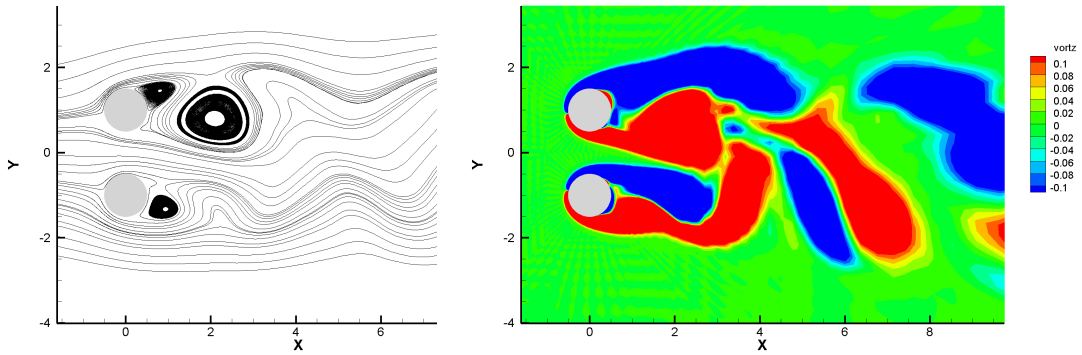

(b) streamlines (b) vorticity

Figure 4.2: Streamlines and vorticity for s=2 when the gap flow is upward or downward biased

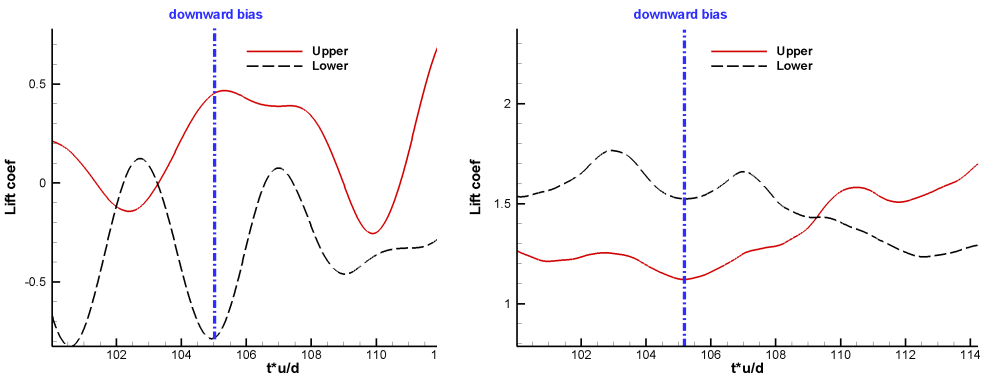

(a) lift coef (b) drag coef

Figure 4.3: Force coefficients at the time instant when the gap flow is deflected downwards for s=2

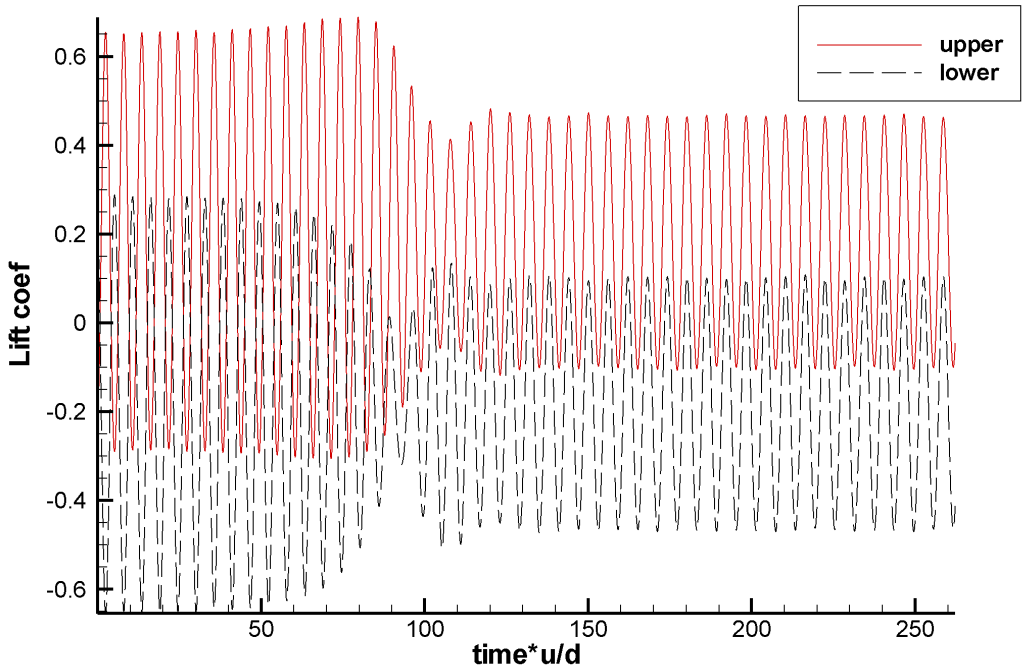

Figure 4.4: Transition from anti-phase regime to in-phase regime for flow past two cylinders s=2.5 and Re=100

and vorticity contour for four different phases defined in figure 4.6. At phase a, the fluid which flows from the bottom side of the cylinders forms a pair of vortices with identical size as shown in the streamlines. At this time instant, both cylinders are having negative lift force. Further downstream when $5 \leq x$, vortices from upper and bottom merge across the centerline to form elongated single vortex and simultaneously two vortex streets merge to a single wide vortex street. Similarly, at phase b, the fluid which flows from the top side of cylinders start to form vortices in proximity of top corners of cylinder pair. These vortices grew bigger and lead to two positive lift forces for both cylinders at time instant of phase c. As the two big vortices convecting away, C_l decreases as shown for phase d. A dramatic feature of these phases is that upper and lower cylinders are having nearly identical flow structures in their near wakes at any time instant. At this spacing, vortex shedding patterns from two cylinders are strongly synchronized to form an exactly anti-symmetrical wake pattern.

Figure 4.8 shows the Mach number distribution of the asymmetric in-phase vortex shedding at Re=100 and s=3d. The gap high-Mach region ($0 \leq x \leq 4$) starts to fluctuate in the transverse direction. In the further downstream along the center line, there is

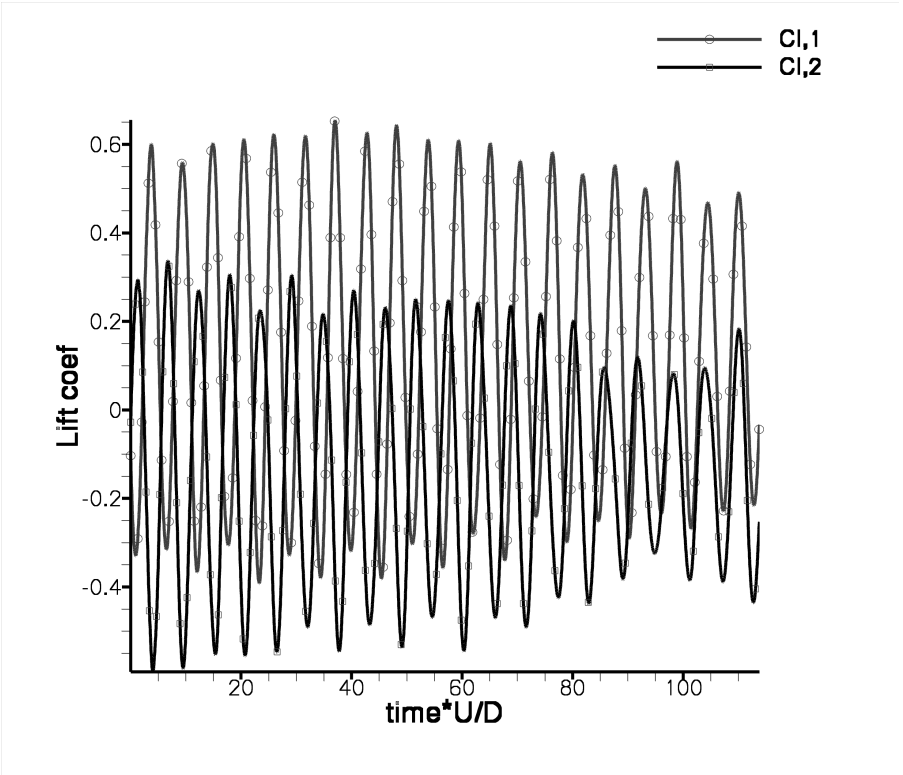

Figure 4.5: Transition from anti-phase regime to in-phase regime for flow past two cylinders s=3 and Re=100

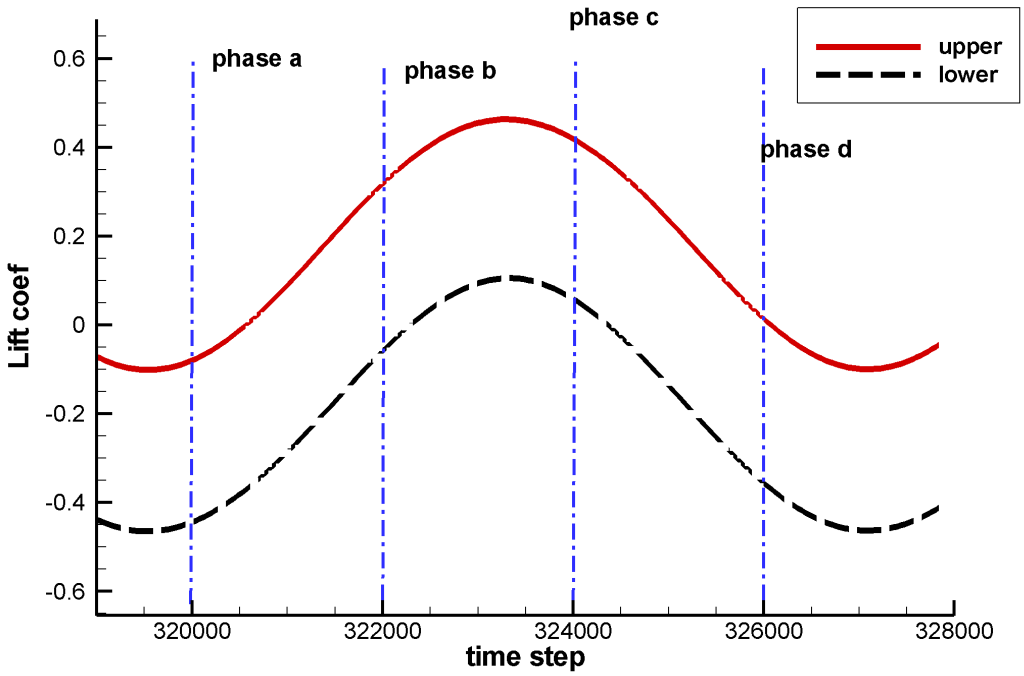

Figure 4.6: Definition of four-phase snopshots for an in-phase vortex shedding flow period of flow past two cylinders with s=2.5 and Re=100

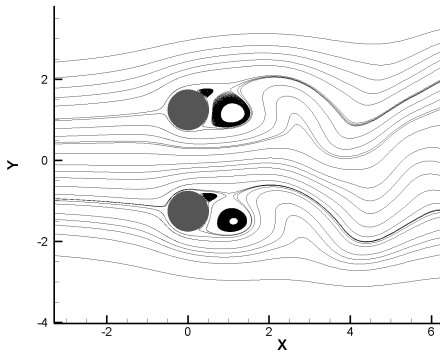

(a) streamlines at phase a

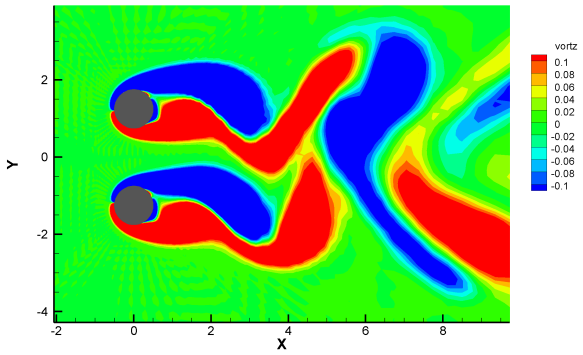

(b) vorticity at phase a

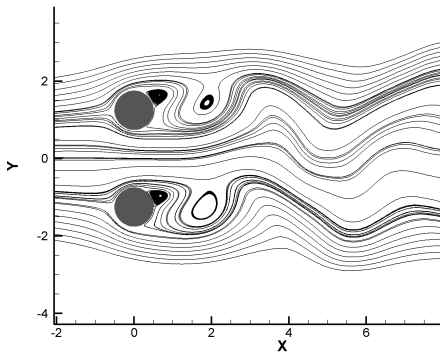

(c) streamlines at phase b

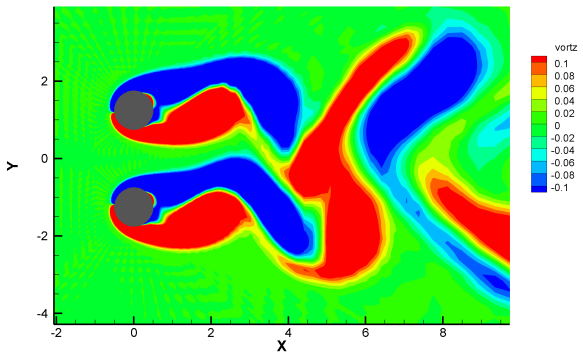

(d) vorticity at phase b

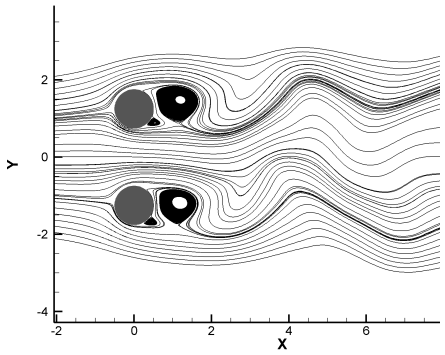

(e) streamlines at phase c

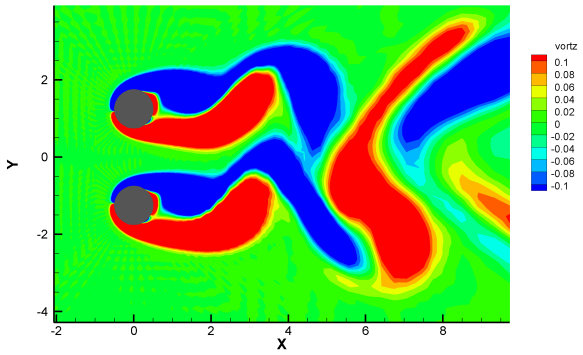

(f) vorticity at phase c

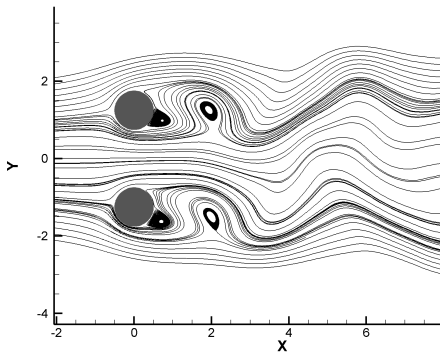

(g) streamlines at phase d

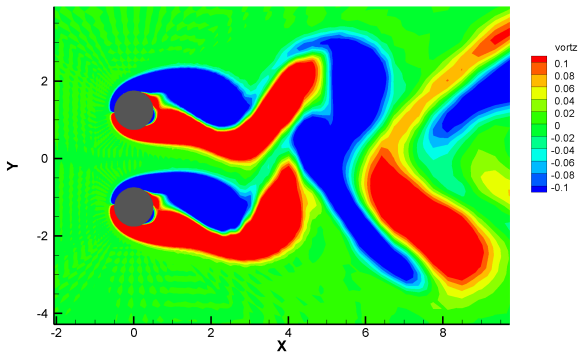

(h) vorticity at phase d

Figure 4.7: Streamlines and vorticity for s=2.5

a continuous low-Mach number distribution. Figure 4.9 shows the spanwise vorticity distribution of the asymmetric in-phase vortex shedding at Re=100 and s=3d. In between x=6 and x=13, there is no longer symmetric pairs of opposite-sign vortices as they are merged into elongated single vortices in the transverse direction. Further downstream ($x \leq 13$), the central line region is associated with a low-magnitude vorticity. Figure 4.10 presents the streamlines of the antisymmetric in-phase vortex shedding at Re=100 and s=3d. The vertex rows merge through a combination of vortices of the same sign with a fluctuating middle stream line, as Williamson (1985) has shown using flow visualization methods. In the downstream region, the merged vortex rows form a single vertex street as already observed in the vorticity contour.

There is a phase difference of 180°for the case of s=3.4 and Re=100 as shown in the figure 4.11. Phase b corresponds to a minimum and a maximum C_l time instant for lower and upper cylinders respectively. Figure 4.12 visualizes the streamlines and vorticity contour for three different phases defined in figure 4.11. The anti-phase vortex shedding pattern is very stable and maintains a long time period as the upper cylinder wake does not seem to interact with the one of the lower cylinder.

Despite the difference predicted for the transitional regime at s=3 by different numerical methods in published literatures, it is generally agreed that s=4 has a symmetric anti-phase synchronized vortex shedding by all the previous numerical studies (Chang and Song (1990); Meneghini et al. (2001); Kang (2003); Ding et al. (2007)). SD method also predicts a very stable symmetric vortex shedding as shown in figure 4.13. The wake patterns of streamlines and vorticity are very close to the ones of $s = 3.4$.

4.3 Flow statistics

Having observed the different flow patterns for different spacings s at Reynolds number 100, attention is now turned to study the impact of s on the statistical force coefficients and Strouhal number.

Figure 4.14 (a) shows the mean C_l for all different spacings. The present results overlap with the data obtained from Ding et al. (2007). The value of mean C_l monotonically decreases towards zero which is the case of an isolated cylinder. There are noticeable

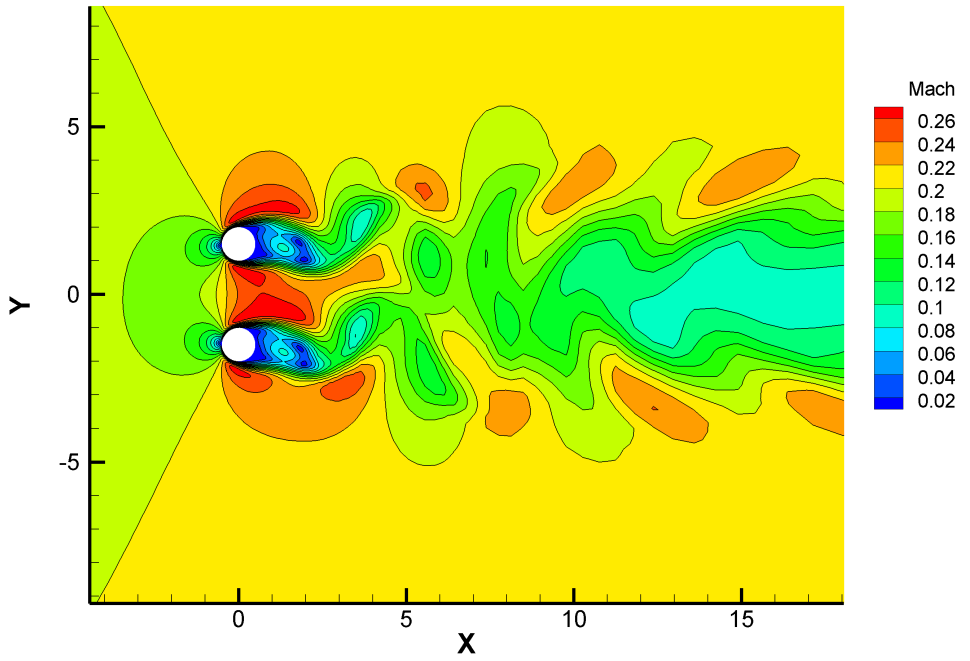

Figure 4.8: Instantaneous Mach number contour computed for flow past two cylinders s=3 and Re=100

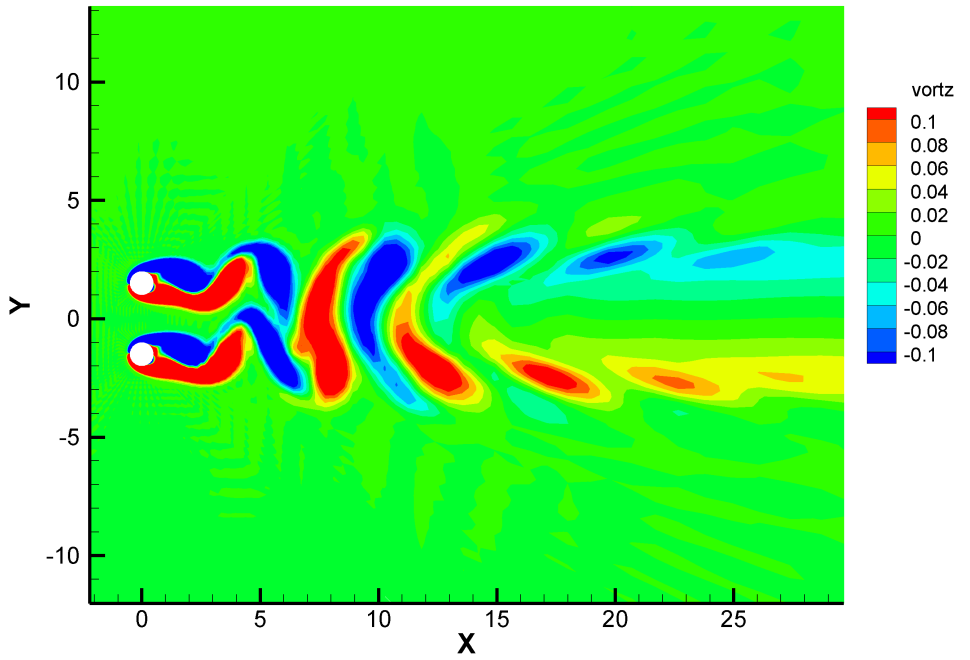

Figure 4.9: Instantaneous vorticity contour computed for flow past two cylinders s=3 and Re=100

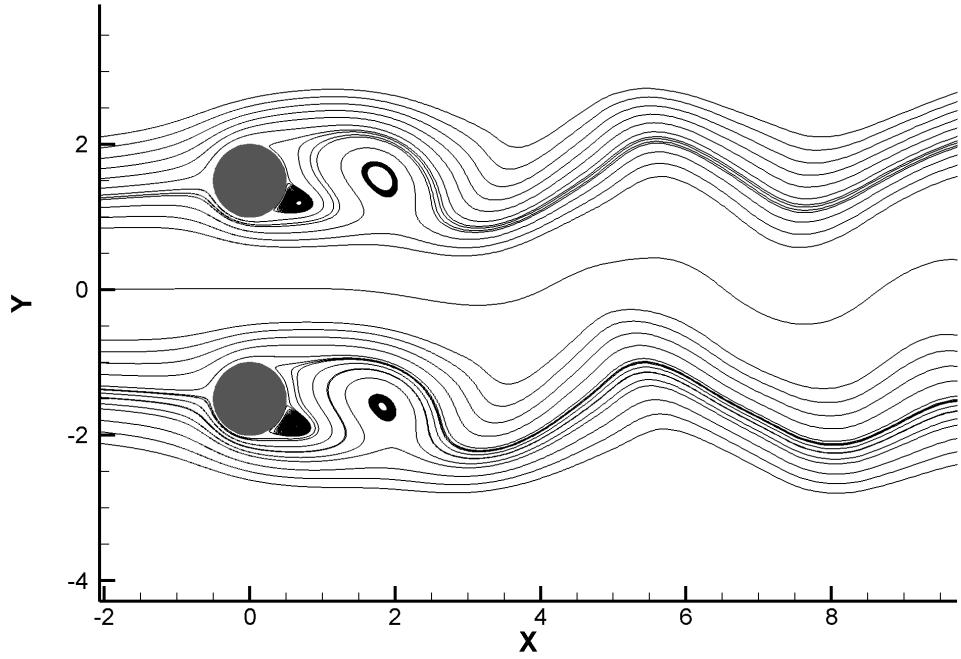

Figure 4.10: Instantaneous streamlines computed for flow past two cylinders s=3 and Re=100

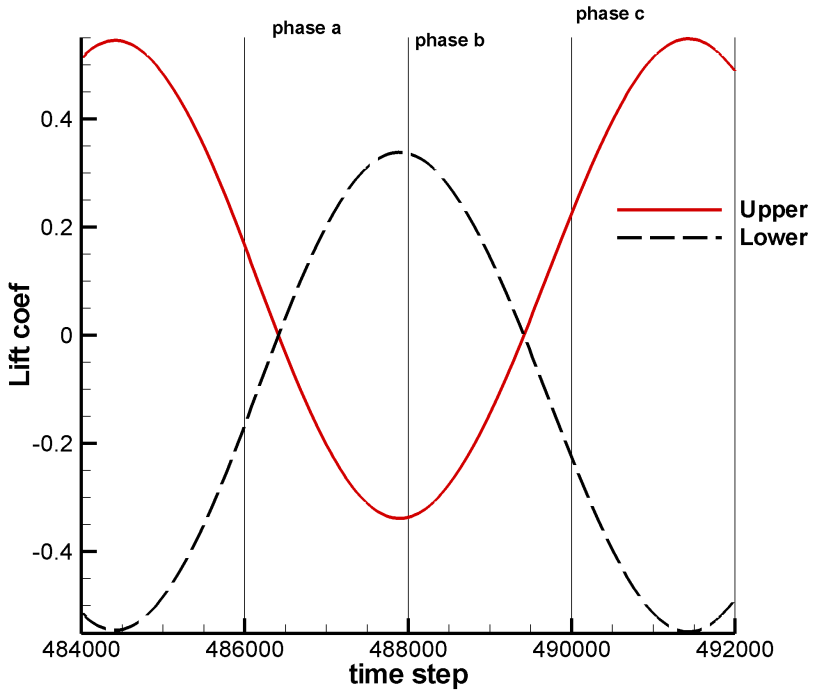

Figure 4.11: Definition of three-phase snopshots for an anti-phase vortex shedding flow period of flow past two cylinders with s=3.4 and Re=100

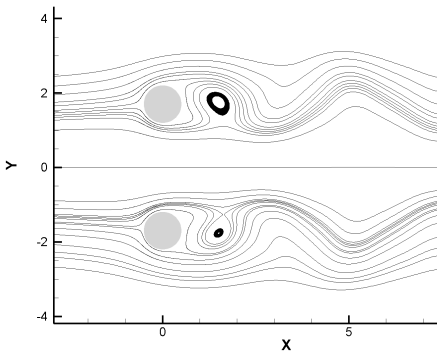

(a) streamlines at phase a

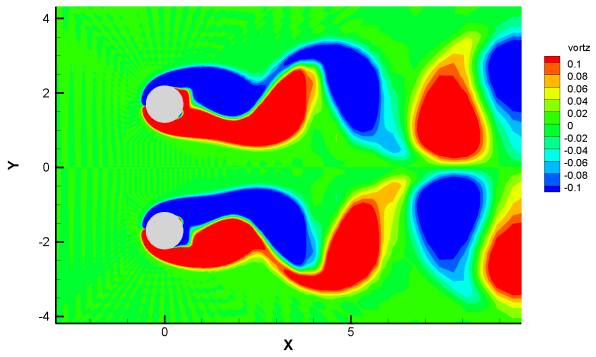

(b) vorticity at phase a

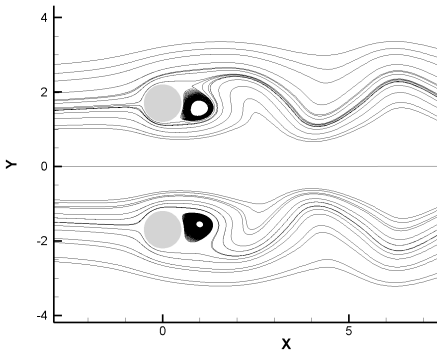

(c) streamlines at phase b

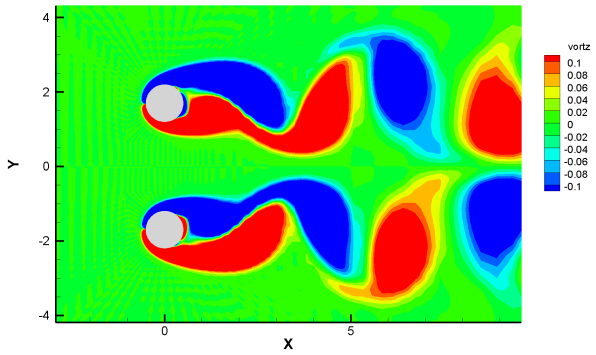

(d) vorticity at phase b

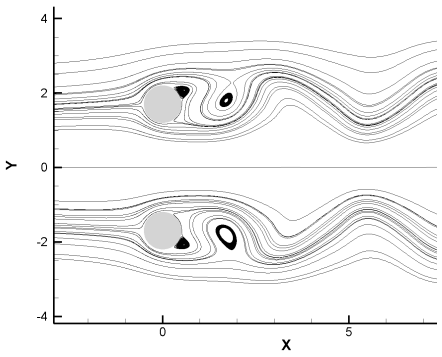

(e) streamlines at phase c

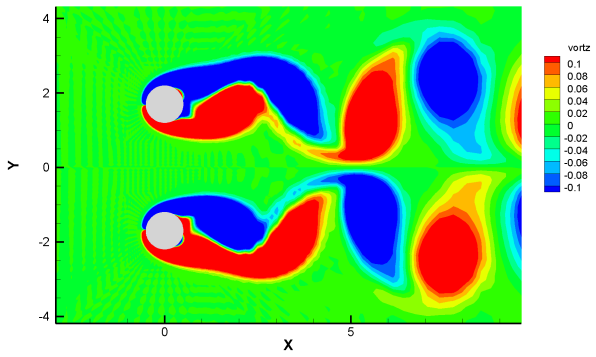

(f) vorticity at phase c

Figure 4.12: Streamlines and vorticity for s=3.4

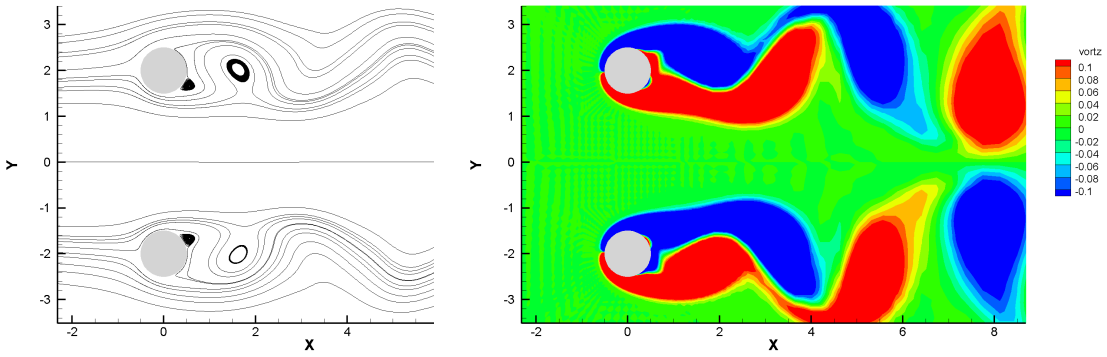

(a) streamlines (b) vorticity

Figure 4.13: Streamlines and vorticity for s=4

differences among the published numerical results for mean C_d as shown in figure 4.14 (b) despite all the values predicted are higher than the one of an isolated cylinder (1.33). As we already discussed, s=2.5 and 3 are associated with in-phase antisymmetric wake pattern, it also induce a mean C_d as low as the flip-flopping asymmetric vortex shedding of s=2. The wake pattern of s=3.4 becomes symmetric and anti-phase synchronized. The values of Kang (2003) show a profile with a maximum at s=3. It deviates a little from our results which project out a peak mean C_d at around s=3.4 which is clearly bigger than the other spacings in figure 4.14 (b).

It is seen from 4.14 (c) that the rms C_l of s=2.5 and 3 (around 0.2) are smaller than those of the other spacings. A sudden increase occurs between s=3 and 3.4 as a result of the change from anti-symmetric to symmetric vortex shedding pattern. It starts decreasing as s increases from 3 to 4 because of the weaker mutual repulsive interaction between two wakes. The rms C_d of figure 4.14 (d) has a sudden decrease from $s = 2$ to 2.5 as a result of upward or downward biased deflections shown in figure 4.2. As s further increases from 2.5, its value reduces slowly. There is generally very much short of published data on rms C_d for side-by-side cylinders. Our present results are in a fair agreement with the ones reported in Ding et al. (2007).

The Strouhal number is also plotted against s in the figure 4.14 (e). Its trend has some similarity to the one for rms C_l. The highest Strouhal number is obtained for s=2 although our predicted value is not as high as the one reported in Kang (2003) as aforementioned. It shows that in-phase synchronized vortex shedding patterns for s=2.5

and 3 are associated with a smaller Strouhal number. A sudden increase happens between $s = 3$ and 3.4 due to the switch of vortex shedding regime and further increase of s to 4 will decrease Strouhal smaller until it approaches the value of an isolated cylinder.

Overall, the predictions of force coefficients and Strouhal numbers reflect correctly the flow physics mode change. They have a strong dependence on spacing s.

4.4 Reynolds number dependence

Having predicted the anti-symmetric flow pattern for Re=100 at s=3 and having noted that Zhou et al. (2001) instead observed symmetric flow pattern for Re=150, we performed two-dimensional simulations of the same flow (s=3) at Reynolds numbers 150 and 200. The synchronization for vortex shedding can be observed from the time history of drag coefficients shown in figure 4.15. This is in a good agreement with the symmetric wake pattern visualized by Zhou et al. (2001). The upper and lower cylinders are having nearly the same C_d both in phase and magnitude.

Figure 4.16 shows the difference of mean C_l, C_d and r.m.s. C_l, C_d as well as the Strouhal number of the upper cylinder for Reynolds numbers 100, 150 and 200. As the Reynolds number increases, the mean C_l decreases but all other values increase. It is also noted that the rms values of force coefficients are generally smaller than those predicted by other simulations (using low-order accurate schemes). The Strouhal number distribution has a fair agreement with other numerical studies. It has big jump between Re 100 and 150 and then increases slowly between 150 and 200. One can also compare them to the experimental values for single cylinder presented by Williamson (1989, 1991). The cylinder pair only has a little higher Strouhal numbers compared to the isolated cylinders at Re 100 and 200 respectively. The present predicted Strouhal number lies just in between the ones predicted by Meneghini et al. (2001) and Ding et al. (2007) for Re 200.

Figure 4.17 shows the Mach number distribution of the symmetric anti-phase vortex shedding at Re=200 and s=3. Along the central line, high and low values of Mach number are alternatively distributed. In particular, these high-Mach zones are surrounded completed in all directions by low-Mach regions. They do not fluctuate in the transverse direction and they are indeed different from the fluctuating ones in figure 4.8. Figure 4.18

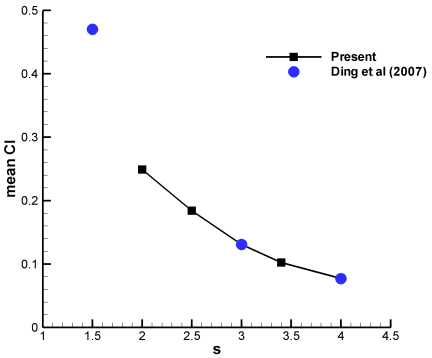

(a) mean C_l

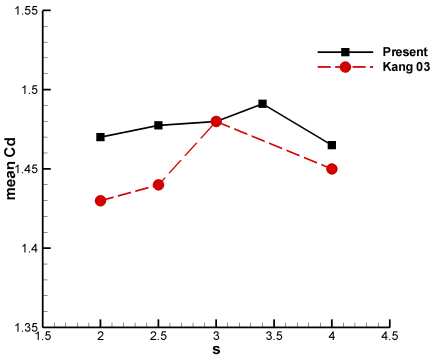

(b) mean C_d

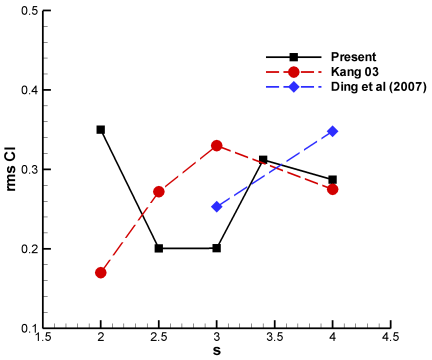

(c) rms C_l

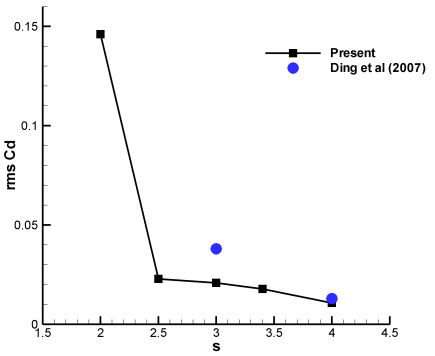

(d) rms C_d

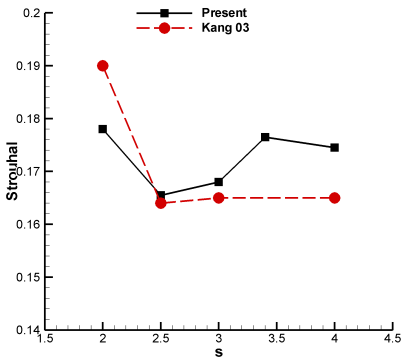

(c) Strouhal no.

Figure 4.14: Spacing dependence for force statistics and Strouhal number

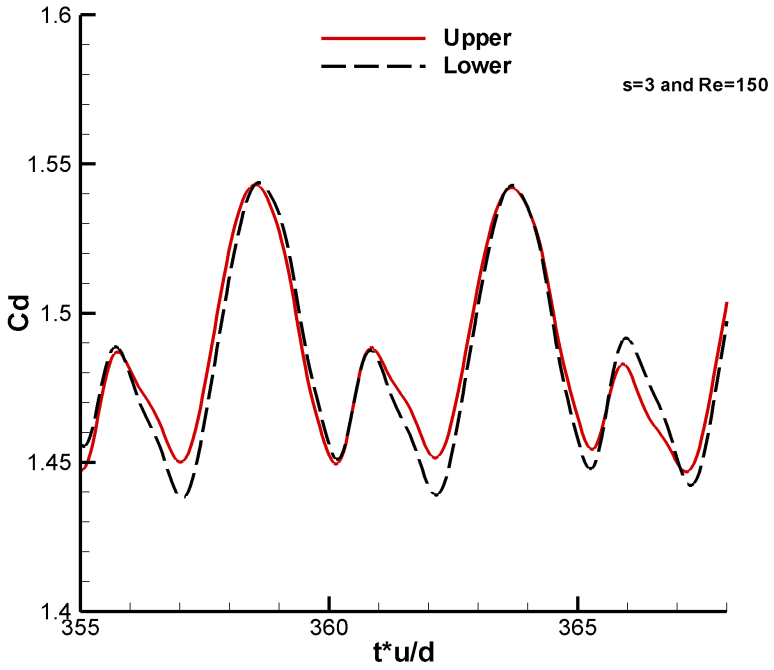

Figure 4.15: Drag coefficient for the case with Re=150 and s=3

shows the spanwise vorticity distribution of the symmetric anti-phase vortex shedding at Re=200 and s=3d. The central line separate more than 10 pairs of symmetric opposite-sign vortices in the region of $0 \leq x \leq 20$. In the near wake ($2 \leq x \leq 15$), adjacent vortices aligned in a straight horizontal line and neighboring vortices are also having opposite signs. Further downstream ($15 \leq x$), in a same streamwise location, there are two pairs of opposite-sign vortices in the transverse direction. In contrast to figure 4.10, figure 4.19 presents the streamlines of the symmetric anti-phase vortex shedding at Re=200 and s=3d. The vertex rows do not merge across the middle straight line.

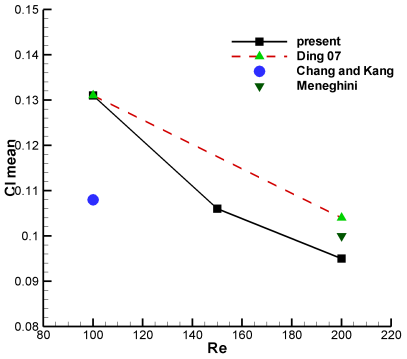

(a) mean C_l

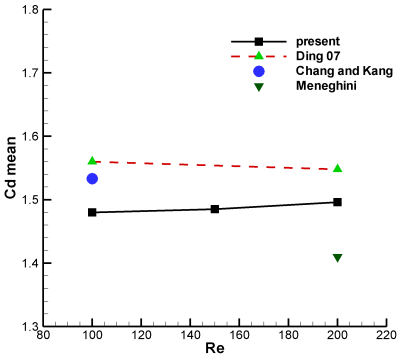

(b) mean C_d

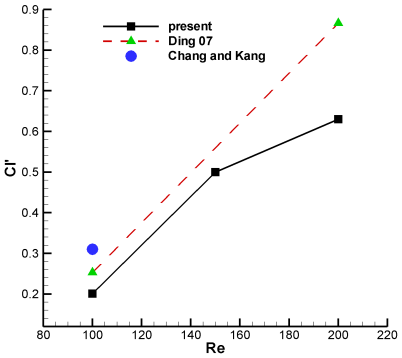

(c) rms C_l

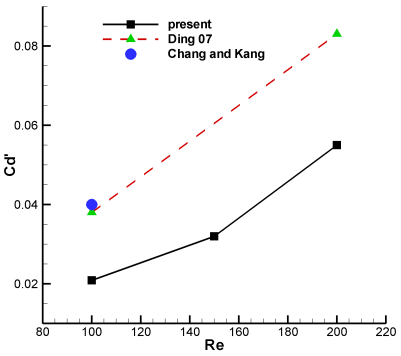

(d) rms C_d

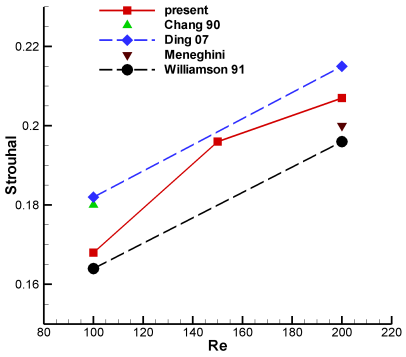

(c) Strouhal no.

Figure 4.16: Reynolds number dependence for force statistics and Strouhal number at s=3

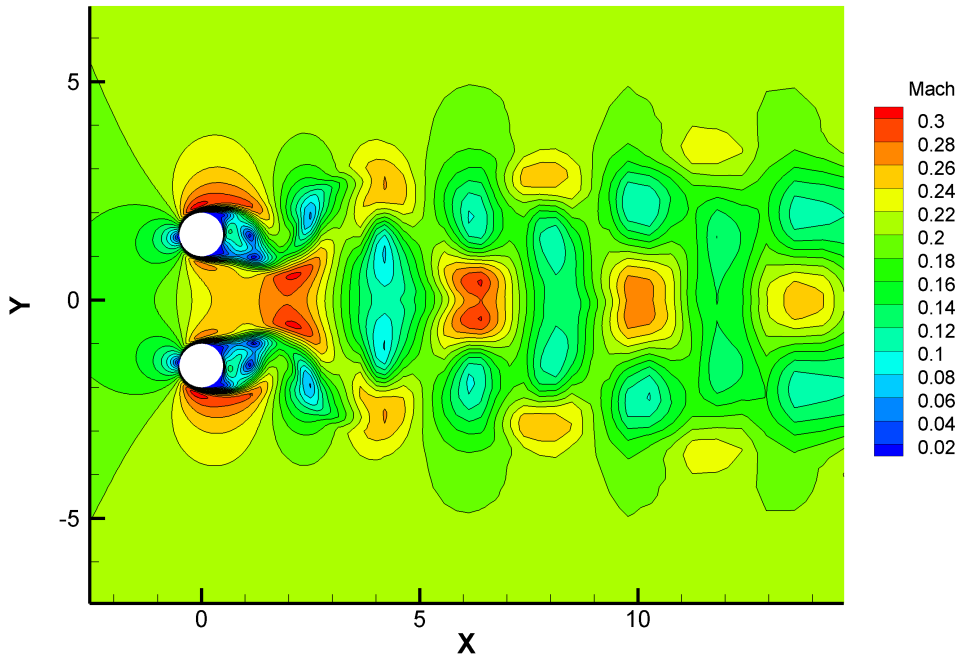

Figure 4.17: Instantaneous Mach number contour computed for flow past two cylinders s=3 and Re=200

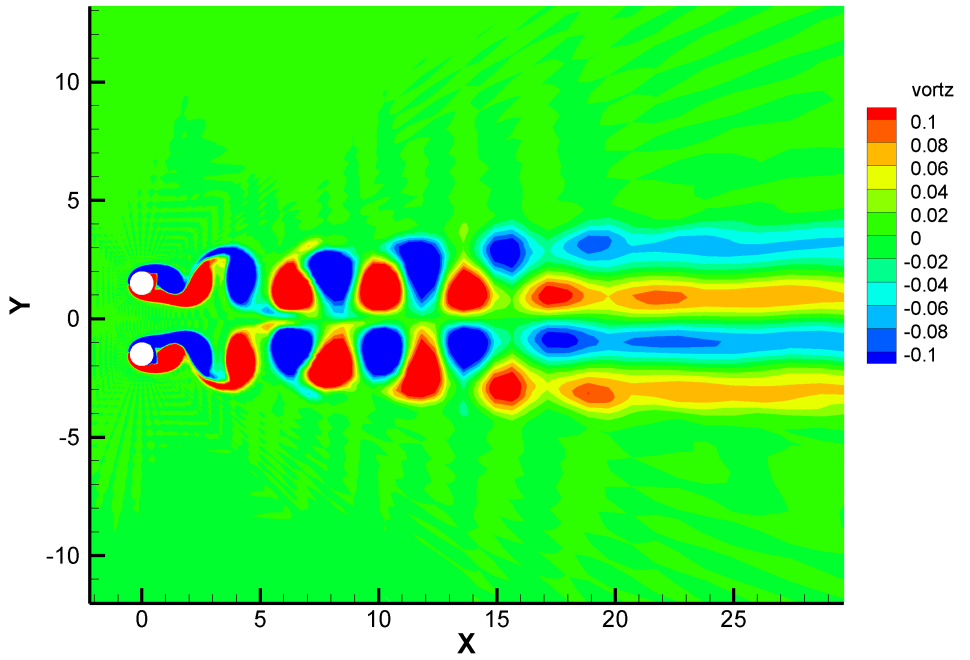

Figure 4.18: Instantaneous vorticity contour computed for flow past two cylinders s=3 and Re=200

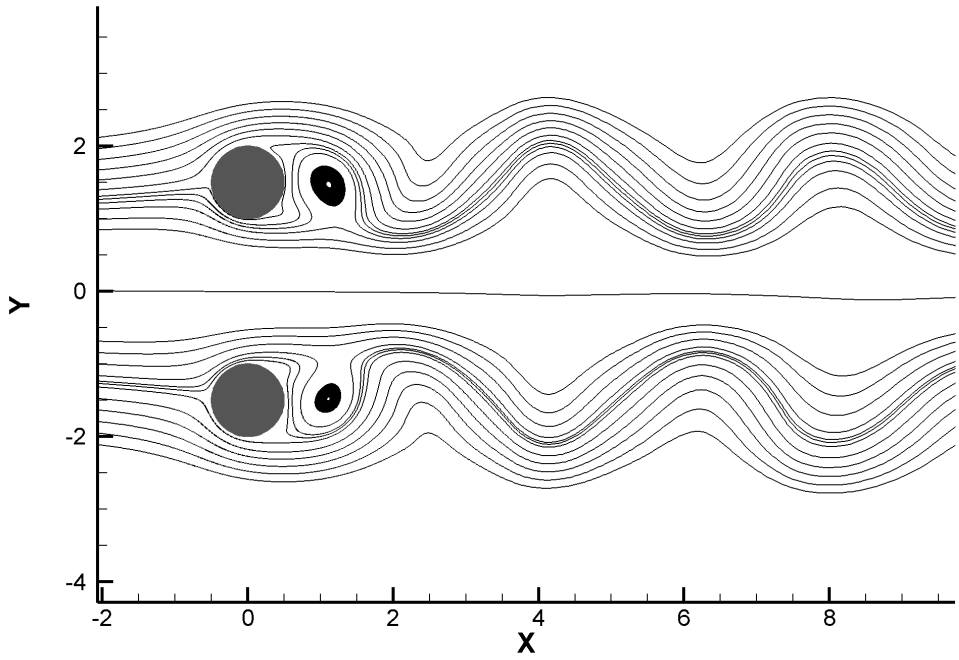

Figure 4.19: Instantaneous streamlines computed for flow past two cylinders s=3 and Re=200

Chapter 5

Conclusion

We have developed a spectral difference solver for inviscid and viscous flows. We verified that our presently developed two-dimensional solver on quadrilateral grids could achieve the desired numerical order on both inviscid and viscous flows. The SD method is then applied to simulate flow past two side-by-side cylinders. At s=2, we predicted an asymmetric flow pattern for flow past the cylinder pair. The anti-symmetric in-phase flow patterns are predicted for arrangements with s=2.5 and 3 at Reynolds number 100. The Reynolds number effect is found significant at s=3 as the unsteady flow still maintain a stable symmetric anti-phase shedding pattern for Reynolds numbers 150 and 200. Further increasing of the distance between two cylinders (s=3.4 and 4), the symmetric anti-phase flow patterns are predicted at Reynolds number 100. Some flow parameters such as the Strouhal number, mean and rms of lift and drag coefficients, which quantitatively characterize the flow fields are produced. They compare well with those of previous studies and reflect the importance of wake pattern flow regime change.

Chapter 6

Acknowledgement

The authors would like to thank the grant supports from NSF and AFOSR. Chunlei Liang also wants to thank Professor Z. J. Wang for discussing about the two-dimensional SD scheme and Andre S. Chan for discussion about some of the flow physics of two side-by-side cylinders.

Bibliography

Bassi, F., Rebay, S. (1997) High-order accurate discontinuous finite element solution of the 2d Euler equations. Journal of Computational Physics 138: 251–285.

Bearmann, P. W., Wadcock, A. J. (1973) The interaction between a pair of circular cylinders normal to a stream. Journal of Fluid Mechanics 61: 499–511.

Chang, K. S., Song, C. J. (1990) Interactive vortex shedding from a pair of circular cylinders in a transverse arrangement. Int. J. for Numer. Methods in Fluids 11: 317–329.

Cockburn, B., Shu, C.-W. (1989) TVB runge-kutta local projection discontinuous galerkin finite element method for conservation laws II: General framework. Mathematics of Computation 52: 411–435.

Cockburn, B., Shu, C.-W. (1998) The runge-kutta discontinuous Galerkin method for conservation laws V: Multidimensional systems. Journal of Computational Physics 141: 199–224.

Ding, H., Shu, C., Yeo, K. S., Xu, D. (2007) Numerical simulation of flows around two circular cylinders by mesh-free least square-based finite difference methods. Int. J. for Numer. Methods in Fluids 53: 305–332.

Huang, Z., Olson, J. A., Kerekes, R. J., Green, S. I. (2006) Numerical simulation of the flow around rows of cylinders. Computers and Fluids 35: 485–491.

Kang, S. (2003) Characteristics of flow over two circular cylinders in a side-by-side arrangement at low Reynolds numbers. Physics of Fluids 15: 2486–2498.

Li, T., Deen, N. G., Kuipers, J. A. M. (2005) Numerical investigation of hydrodynamics and mass transfer for in-line fiber arrays in laminar cross-flow at low reynolds numbers. Chemical Engineering Science 60: 1837–1847.

Liang, C., Kannan, R., Wang, Z. J. (2008) A p-multigrid spectral difference method with explicit and implicit smoothers on unstructured triangular grids. Computers and Fluids in press, doi: 10.1016/j.compfluid.2008.02.004.

Liang, C., Papadakis, G. (2007) Large Eddy Simulation of flow over a staggered tube bundle at subcritical Reynolds number. Journal of Fluids and Structures 23: 1215–1230.

Liu, Y., Vinokur, M., Wang, Z. J. (2006*a*) Spectral difference method for unstructured grids I: Basic formulation. J. of Comput. Phys. 216: 780–801.

Liu, Y., Vinokur, M., Wang, Z. J. (2006*b*) Spectral (finite) volume method for conservation laws on unstructured grids V: Extension to three-dimensional systems. Journal of Computational Physics 212: 454–472.

Meneghini, J. R., Saltara, F., Siqueira, C. L. R., Ferrari, J. A. (2001) Numerical simulation of flow interference between two circular cylinders in tandem and side-by-side arrangements. J. Fluids and Structures 15: 327–350.

Mittal, S., Tezduyar, T. (1998) A unified finite element formulation for compressible and incompressible flows using augmented conservation variables. Computer Methods in Applied Mechanics and Engineering 161: 229–243.

Rusanov, V. V. (1961) Calculation of interaction of non-steady shock waves with obstacles. Journal of Computational Math Physics USSR 1: 261–279.

Sharman, B., Lien, F. S., Davidson, L., Norberg, C. (2005) Numerical predictions of low reynolds number flows over two tandem circular cylinders. Int. J. for Numerical Methods in Fluids 47: 423–447.

Spiteri, R. J., Ruuth, S. J. (2002) A new class of optimal high-order strong-stability-preserving time discretization methods. SIAM J. Numer. Anal. 40: 469–491.

Sun, Y., Wang, Z. J., Liu, Y. (2006) Spectral (finite) volume method for conservation laws on unstructured grids VI: extension to viscous flow. Journal of Computational Physics 215: 41–58.

Sun, Y., Wang, Z. J., Liu, Y. (2007) High-order multidomain spectral difference method for the navier-stokes equations on unstructured hexahedral grids. Communication in Computational Physics 2: 310–333.

Wang, Z., Liu, Y., May, G., Jameson, A. (2007) Spectral difference method for unstructured grids II: Extension to the euler equations. Journal of Scientific Computing 32: 45–71.

Wang, Z. J. (2002) Spectral (finite) volume method for conservation laws on unstructured grids: I Basic formulation. J. of Comput. Phys. 178: 210–251.

Wang, Z. J., Liu, Y. (2006) Extension of the spectral volume method to high-order boundary representation. Journal of Computational Physics 211: 154–178.

Williamson, C. H. K. (1985) Evolution of a single wake behind a pair of bluff bodies. Journal of Fluid Mechanics 159: 1–18.

Williamson, C. H. K. (1989) Oblique and parallel modes of vortex shedding in the wake of a circular cylinder at low Reynolds numbers. Journal of Fluid Mechanics 206: 579–627.

Williamson, C. H. K. (1991) 2d and 3d aspects of the wake of a cylinder, and their relation to wake computations. Lectures in Applied Mathematics 28: 719–751.

Zdravkovich, M. M. (1977) Review of flow interference between two circular cylinders in various arrangements. ASME Journal of Fluids Engineering 99: 618–633.

Zdravkovich, M. M. (1987) The effects of interference between circular cylinders in cross flow. Journal of Fluids and Structures 1: 239–261.

Zhou, Y., Wang, Z. J., So, R. M. C., Xu, S. J., Jin, W. (2001) Free vibrations of two side-by-side cylinders in a cross flow. Journal of Fluid Mechanics 443: 197–229.